Matched filters for multispectral point target detection

S. Buganim and S.R. Rotman*
Ben-Gurion University of the Negev, Dept. of Electro-optical Engineering, Beer-Sheva, ISRAEL

ABSTRACT

Spectral signatures derived from a multispectral or hyperspectral imager can be used in matched filter algorithms to help distinguish targets from background. In this paper we demonstrate the use of these matched filters for different target implantation models. We show that even though a specific matched filter is designated for a particular implantation model, we can use other matched filters and obtain higher detection values for low false alarm rates. We evaluate the efficiency of the algorithms by systematically implanting the target's signature into every pixel in the image and obtaining its score; the lowest scores are those pixels in which the target may be missed. For every algorithm, we generate histograms for the no-target and target cases and then analyze using the classical ROC curve.

Keywords: Point target detection, multispectral imagery

1. INTRODUCTION

In the world of target detection, many sophisticated techniques have been developed to detect point targets in natural backgrounds [1]-[4]. With the advent of multi- and hyper-spectral cameras, we believe the spectral domain will become a necessary component of many point target detection algorithms. Target detection can be applied even when no target information is available by using anomaly detection algorithms. The standard method in the literature of detecting point anomalies in multispectral data is based on the RX algorithm [5]. The RX algorithm is a constant false-alarm rate (CFAR) detector, which is derived from a generalized-likelihood ratio test (GLRT).

In cases where target information exists, target detection algorithms usually try to match the target's signature to the suspect pixel and suppress the background. These algorithms are frequently referred to as matched filters. In this paper we will examine different matched filters for specific models of target implantation and explore the use of non-optimal filters for detection.

2. POINT TARGET DETCETION ALGORITHMS

Anomaly detection algorithms that are used in cases where no target information is available extract targets whose spectral signatures are distinct from their surrounding. A widely used anomaly detector for multispectral data is the algorithm presented in [5], commonly referred to as the RX algorithm, after the initials of its developers Reed and Xiaoli Yu. For each image pixel vector $\vec{x}'$ the RX detector implements an anti-mean filter specified by

$$r = (\vec{x}' - \vec{m})^T \vec{\vec{\Phi}}^{-1} (\vec{x}' - \vec{m}) \tag{1}$$

where $\vec{m}$ is the estimated local mean, implemented by us as the average of the eight surrounding pixels, and the spectral covariance matrix, $\vec{\vec{\Phi}}$, is estimated from the overall data cube. We implicitly assume that a few targets in the data cube will not noticeably affect our estimate of the spectral covariance matrix.

In cases where the target signature is known [6]-[7], we must decide how the target is implanted into the image. Let us assume that $\vec{x}$ is the pixel without the target. If the target when present was substitutive of the form (where p is the fraction of the pixel replaced by the target)

$$\vec{x}' = (1-p)\vec{x} + p\vec{t} \tag{2}$$

* srotman@ee.bgu.ac.il

Imaging Spectrometry XI, edited by Sylvia S. Shen, Paul E. Lewis,
Proc. of SPIE Vol. 6302, 63020Z, (2006) · 0277-786X/06/$15 · doi: 10.1117/12.678168

then for the matched filter, equation (1) would become:

$$r = \left(\vec{t} - \vec{m}\right)^T \cdot \vec{\vec{\Phi}}^{-1} \cdot (\vec{x}' - \vec{m}) \tag{3}$$

where $\vec{t}$ is the target signature.

On the other hand, if the target was additive, i.e.

$$\vec{x}' = \vec{x} + p\vec{t} \tag{4}$$

then

$$r = \vec{t}^T \cdot \vec{\vec{\Phi}}^{-1} \cdot (\vec{x}' - \vec{m}) \tag{5}$$

Although each implantation has its own matched filter, we could use each of the filters specified by equations (3) and (5) for both implantations given in (2) and (4), and compare the results that they produce.

3. EVALUATING ALGORITHMS

To evaluate the algorithms over a wide spectrum of targets and target locations, we embedded point targets in our multispectral data sets, as described above. We compare the efficacy of the two algorithms for particular target strength by using classical Receiver Operating Characteristic (ROC) curves. The technique is as follows (as described in Bar-Tal and Rotman as given in Ref. 3): first we operate on the raw data, i.e., without any embedded targets. We evaluate for each pixel the algorithm being tested using Equation (3) or Equation (5). The results are summarized in what we call a no-target histogram. Next we embed targets into every pixel location and evaluate the algorithm under study. This is done independently for each pixel location (rather than simultaneously) so that surrounding pixels are not changed prior to the algorithm evaluation. The results are placed in a target histogram. For each histogram (no-target and target) the following steps are taken. Each histogram is normalized and a cumulative probability histogram is calculated. Subsequently one minus the value of the cumulative probability histogram is computed giving us the inverse cumulative probability distributions for both the no-target and target cases. The x-axis of these distributions are the values of r from equations (3) and (5); the y-axis is the value of the probability of false alarm and the probability of detection taken from the no-target and target-present inverse cumulative probability distribution, respectively, for that value. For each threshold in the histograms we obtain a pair of values corresponding to the probability of detection and probability of false alarm; and using these pairs we generate our ROC curve.

To summarize, the steps to evaluate the ROC curves are as follows:

1. Run the algorithm on the data cube with an embedded target in every pixel location. (The target is not in all the positions simultaneously; rather the result is obtained sequentially.)
2. Generate a histogram of the algorithm result for embedded targets.
3. Generate a cumulative histogram of the algorithm result for embedded targets. (Normalize to number of pixels evaluated.)
4. Generate an inverse cumulative probability distribution (1.0-cumulative histogram), using result from step 3. (These are the Probability of Detection (P_D) values.)
5. Run the algorithm on the original data cube in which no targets have been implanted.
6. Generate a histogram of the algorithm result for no targets. (Use same scale as step 2.)
7. Generate a cumulative histogram of the algorithm result for no targets. (Normalize to number of pixels evaluated)
8. Generate an inverse cumulative probability distribution (1.0-cumulative histogram), using result from step 7 (These are the Probability of False Alarm (P_{FA}) values.)
9. Plot the Probability of Detection values (step 4) versus Probability of False Alarm values (step 8).

One weakness to this method of comparing algorithms is that the scales of both the probability of false alarms and the probability of detection go from 0 to 1. Thus, a false alarm and a missed detection are equally weighted.

In many applications, the probability of false alarms must be kept down very low; the probability of detection does not have to be equivalently high. Thus, we have decided to run our algorithm for comparing detection and false alarm with ROC curves that extend from 0 to 1 for the probability of detection, but 0 to a low value (judiciously chosen) for the probability of false alarms.

4. DATA DESCRIPTION

The results to be presented were performed on multispectral cubes found in Refs. 8 and 9. The cube to be presented was the one labeled Fig. 7 in the site listed at Ref. 9. There were 30 bands in the cube spanning the visible wavelengths from 400 to 720 nm. The pixel (473,403) was used as a target. Further details can be found in Refs. 8 and 9.

5. RESULTS

Let us start by analyzing the standard algorithm given in Equation (5). The histograms are shown in Fig. 1. The following results can visually be seen and theoretically calculated.

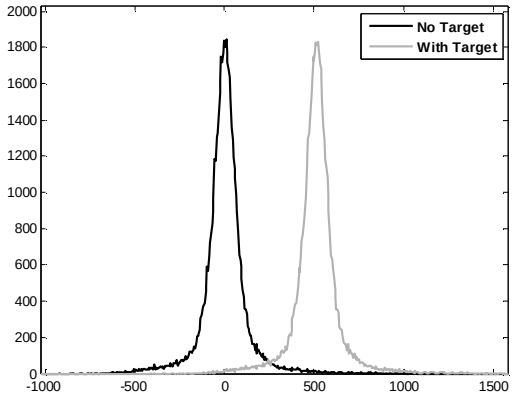

Fig. 1 – No-Target and With-Target Histograms for Equation (5)

1. The two histograms are identical and shifted versions one of the other.
2. The mean of the no-target histogram is 0.
3. The variance of the no-target (NT) histogram and of the with-target (WT) histogram are both equal to $\vec{t}^{T} \cdot \vec{\vec{\Phi}}^{-1} \cdot \vec{t}$.
4. The mean of the with-target histogram is $p\vec{t}^{T} \cdot \vec{\vec{\Phi}}^{-1} \cdot \vec{t}$.
5. Both histograms exhibit long tails in both the positive and negative directions. Experience has shown that these tails are coming from areas of high variability (e.g. edges), where the estimate of $\vec{m}$ is particularly poor.

We can compare these histograms to theoretical Guassian curves defined by the measured means and variances. Fig. 2 shows a log normal probability plot of the actually measured curve vs. the theoretical curve. Fig. 3 shows the theoretical and experimental normalized histograms themselves. It can be seen that the experimental curves exhibit the characteristic long tails.

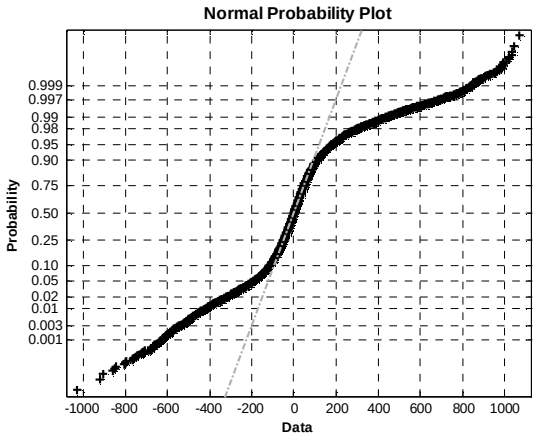

Fig. 2 – Normal Probability Plot for both NT & WT Histograms in Fig. 1

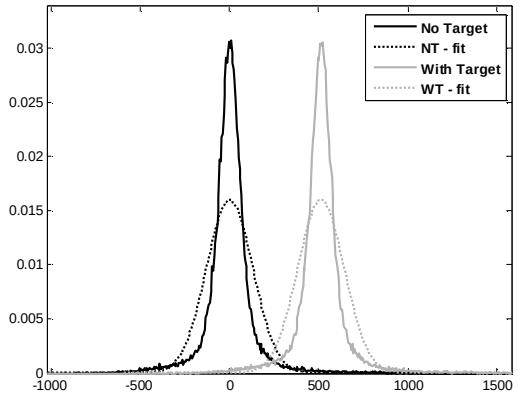

Fig. 3 – NT & WT Normalized Histograms and their fit, for Equation (5)

Another way to compare the algorithms is to consider the Battarcharya Distance between the two histograms f(x) and g(x). Each histogram is normalized to 1; the distance is given by

$$D_{dist} = -\ln \int_{-\infty}^{\infty} \sqrt{f(x)g(x)}dx \tag{6}$$

Note that if the histograms are identical, then the result is 0. For the histograms shown in Fig. 3, the result was 0.05.

As can be seen from the resulting ROC curve given in Fig. 4, the actual ROC curve's performance is somewhat inferior to what we could have achieved from a perfect Gaussian distribution.

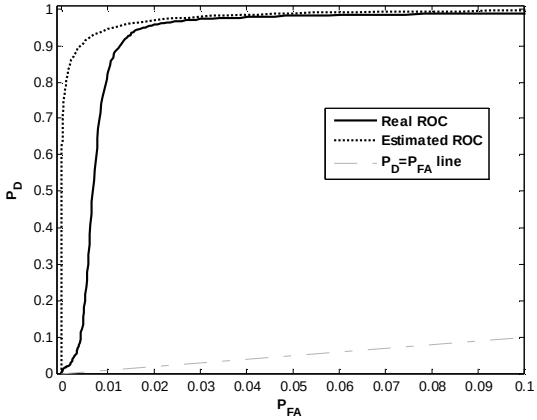

Fig. 4 – Estimated and Real ROC Curves, for Equation (5)

Let's apply the algorithm presented in Equation (3) for an additive implantation model. Notice that the algorithm is not the optimal matched filter for this case. Furthermore, we cannot use this algorithm without applying an absolute value operation because adding a target to a pixel could produce higher negative results. The modified algorithm is

$$r = \left| \left(\vec{t} - \vec{m}\right)^T \cdot \vec{\vec{\Phi}}^{-1} \cdot \left(\vec{x}' - \vec{m}\right) \right|. \tag{7}$$

Applying the above algorithm to an additive model implantation yields the histograms shown in Fig. 5.

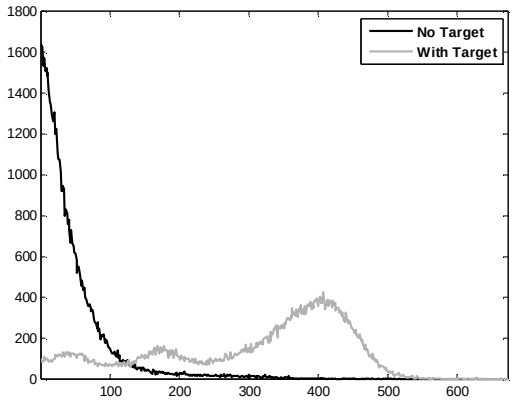

Fig. 5 – No-Target and With-Target Histograms for Equation (7)

Although we could calculate the expected values and variances of the no-target and target histograms shown in Fig. 5, that is not the appropriate approach to understanding the underlying behavior of these histograms. As we can see, the target histogram exhibits multimode Gaussian distributions and therefore should not be treated as a single mode, as shown in Fig. 6. We can see that the deviation from a single mode Gaussian is quiet substantial. Figure 7 also demonstrates this by showing the estimated ROC curve that is generated from the fitted histograms shown in Fig. 6 versus the real ROC curve.

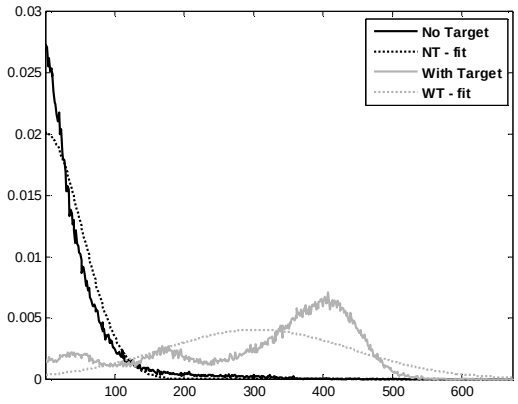

Fig. 6 - NT & WT Normalized Histograms and their fit, for Equation (7)

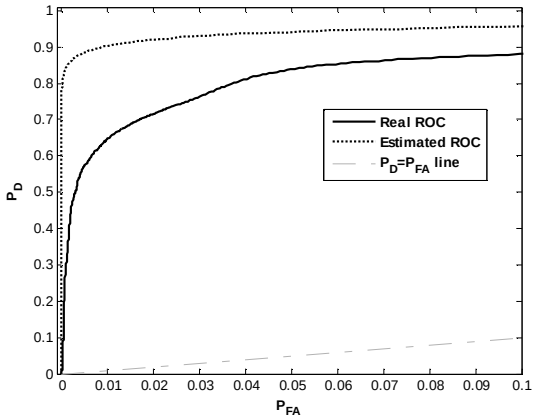

Fig. 7 - Estimated and Real ROC Curves, for Equation (7)

We can use segmentation as an explanation to the multimode Gaussian behavior of the histograms shown in Fig. 5. The different segments in the multispectral image causes separate groups of values from Equation (7) to unite around specific values. These values can be obtained from reanalyzing Equation (7). Let's start by rewriting this equation as

$$r = \left| \left(\vec{t} - \vec{\mu}_L\right)^T \cdot \vec{\vec{\Phi}}^{-1} \cdot (\vec{x}' - \vec{m}) + \left(\vec{\mu}_L - \vec{m}\right)^T \cdot \vec{\vec{\Phi}}^{-1} \cdot (\vec{x}' - \vec{m}) \right| \tag{8}$$

where $\vec{\mu}_L$ is the segment's mean.

If we assume that the fluctuations in Equation's (8) second term are negligible, we can easily estimate the expected value as $\left| p\left(\vec{t} - \vec{\mu}_L\right)^T \cdot \vec{\vec{\Phi}}^{-1} \cdot \vec{t} \right|$ and the variance as $\left(\vec{t} - \vec{\mu}_L\right)^T \cdot \vec{\vec{\Phi}}^{-1} \cdot \left(\vec{t} - \vec{\mu}_L\right)$. Fig. 8 shows the different segments distributions and their estimated histograms that were generated from the expected value and variance given above. As shown, this estimation is fairly appropriate.

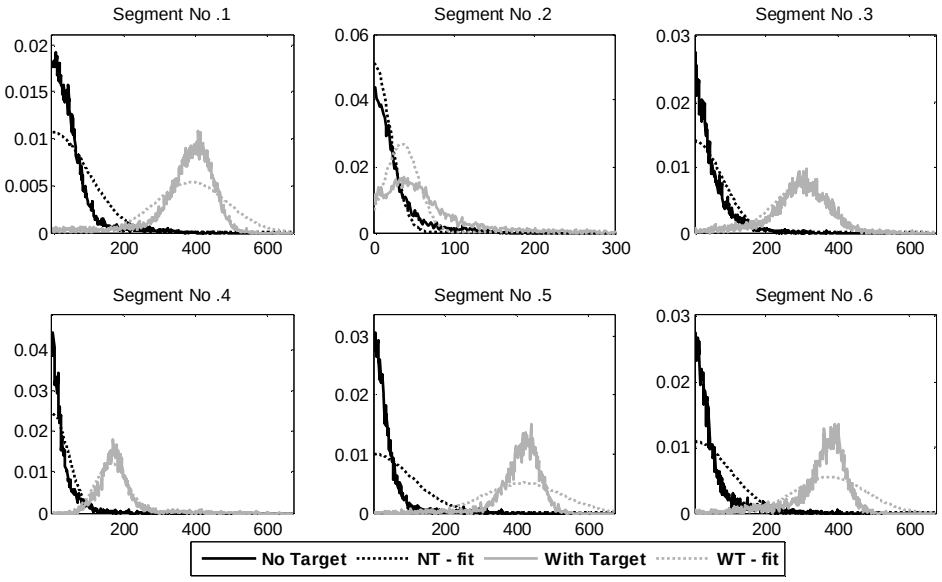

Fig. 8 - NT & WT Normalized Histograms for Six Segments and their fit, based on Equation's (8) approximation

We would now like to check and see if the approximation based on segmentation (multimode) can yield more accurate ROC curves than the ones based only on overall expected values and variances (singlemode). In order to generate a ROC curve from the approximated histograms shown in Fig. 8 we need to add them up according to their weights. These weights are calculated from the number of pixels that generated each histogram (the number of pixels in a given segment) divided by the total number of pixels in the image. Figure 9 shows the actual and the theoretical histograms, based on multimode Gaussian (the segmentation approach). Figure 10 shows the corresponding ROC curves.

Using segmentation in order to approximate the algorithm's behavior is indeed the proper approach, as can be seen from comparing figs. 6&7 to 9&10.

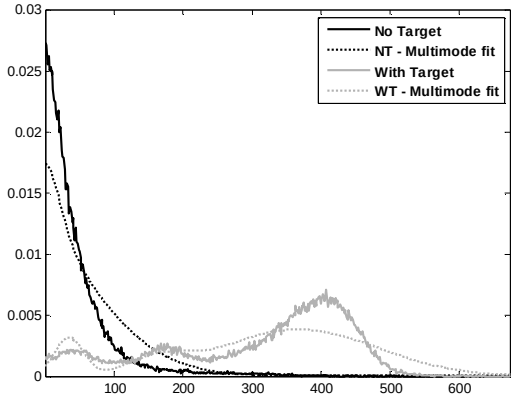

Fig. 9 - NT & WT Normalized Histograms and their Multimode fit, for Equation (7)

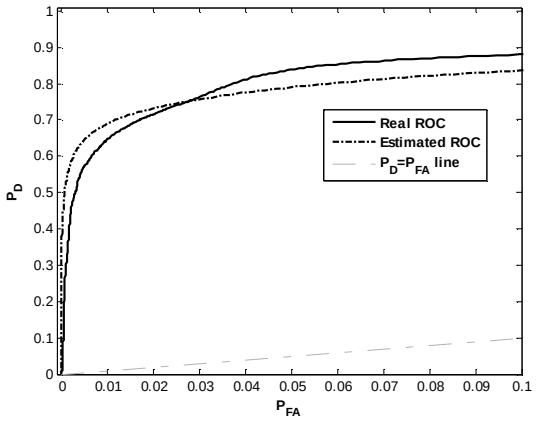

Fig. 10 - Estimated (Multimode) and Real ROC Curves, for Equation (7)

6. ALGORITHMS COMPARISON

Each one of the algorithms presented in equations (3) and (5) is a matched filter for a specific model of implantation (substitutive or additive, respectively). Figs. 5 through 10 present the results obtained from applying the "wrong" matched filter to an additive model, i.e. the substitutive model's matched filter. Figure 11 shows both models ROC curves. Surprisingly, the addition model's matched filter does not produce better detection for all false alarm rates. Moreover, as noted in section 3, in many cases the probability of false alarm must be kept down very low; thus the non-optimal matched filter is preferable for those applications which require a minimal rate of false alarms.

For a visual comparison of the MF's and non-MF's histograms we need to normalize the histograms on the x-axis as well. We have found that if we normalize according to the no-target histogram's standard deviation we can easily compare between algorithms but since the modified non-MF produces only positive results, we normalize it according to a standard deviation that is calculated from an expected value of zero. Figure 12 presents the algorithms normalized histograms. Note that this normalization has no effect on the shape of the ROC curves.

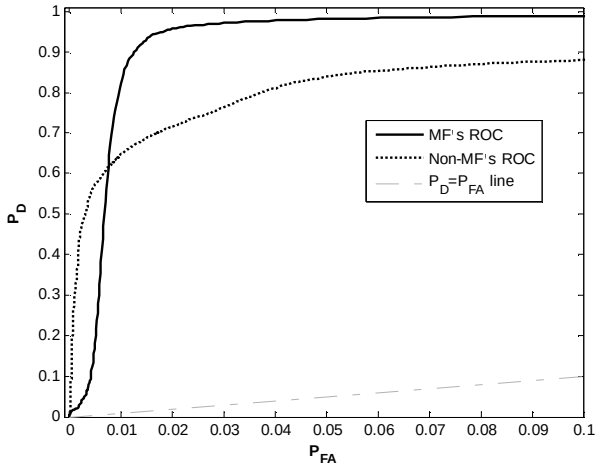

Fig. 11 - ROC curves for addition model implantation, MF's and Non-MF's

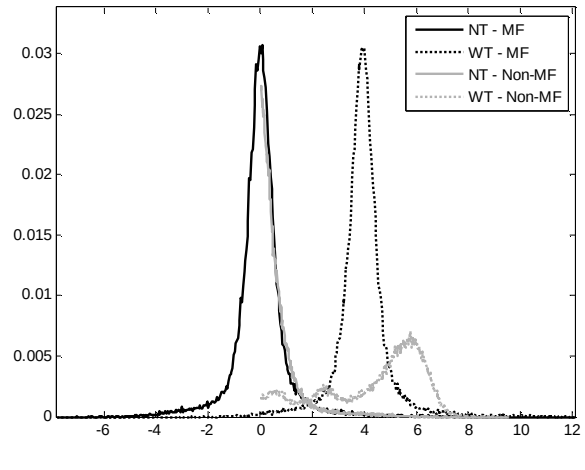

Fig. 12 - Normalized histograms for addition model implantation, MF's and Non-MF's

Figure 12 helps to understand why the matched filter for the addition model's performance is inferior to the non-optimal matched filter under low false alarms. The different segments in the image cause the non-optimal MF's histograms to separate into different groups of values. In segments where the target is very different from the background, the algorithm produces higher values then the ones created from the optimal matched filter. Thus, on very low false alarm rates, we can obtain higher detection values.

7. CONCLUSIONS

We have considered the use of non-optimal matched filter for additive model of target implantation and found that in some cases, we can obtain better detection rates at low false alarm rates. In order to explain the non-optimal algorithm's behavior we used segmentation and found that the cause of its better performance in low false alarm rates is separation due to the different segments in the image.

Our method of evaluating algorithms by implanting targets sequentially assisted our comparison between the two matched filters for the additive model. Future work will include comparison of these matched filters on other target implantation models.

ACKNOWLEDGEMENTS

We'd like to thank Mrs. Charlene Caefer and Dr. Jerry Silverman from the Air Force Research Laboratory for many stimulating discussions. This work was partially supported by the Paul Ivanier Center for Robotics and Industrial Production, Beer-Sheva, Israel. This work was also supported by the U.S. Air Force AFOSR International Research Initiative Grant #037077. All opinions stated in this paper are those of the authors and not of the U.S. Government.

REFERENCES

1. C.-I. Chan and H. Ren, “An Experiment-based quantitative and comparative analysis of target detection and image classification algorithms for hyperspectral imagery”, IEEE Trans. GRS 38(2), pp. 1044-1063, 2000 and references therein.
2. J.S. Acetta, Infrared Electro-Optical Systems Handbook, “Infrared search and track systems,” Chap. 4 in Passive Electro-Optical Systems, V. 5 of the S. B. Campana, Ed., pp. 209-344, ERIM and SPIE, Ann Arbor MI, 1993.
3. M. Bar-Tal and S.R. Rotman, “Performance Measurement in Point Target Detection,” Inf. Phys. Tech., 37, pp. 231-238, 1996.
4. R. Succary, A. Cohen, P. Yarctzi, S.R. Rotman and S. Nadav, “Dynamic Programming Algorithm for Point Target Detection: Practical Parameters for DPA”, in Signal and Data Processing of Small Targets 1992, O.E. Drummond ed. , Proceedings of SPIE Vol. 4473, pp. 96-100, 2001.
5. I. S. Reed and X. Yu, “Adaptive Multiple-Band CFAR Detection of an Optical Pattern with Unknown Spectral Distribution”, IEEE Trans. on Acoustics, Speech, and Signal Processing, 38(10), pp.1760-1770, 1990.
6. C. E. Caefer, S.R. Rotman, J. Silverman, and P.W. Yip, "Algorithms for point target detection in hyperspectral imagery", in Imaging Spectrometry VIII, Sylvia S. Shen ed., Proceedings of SPIE vol. 4816, pp. 242-257, 2002.
7. O. Raviv and S.R. Rotman "Applying ordered statistics filters for point target detection in hyperspectral data", in Signal and Data Processing of Small Targets 2003, O.E. Drummond, Ed., Proceedings of SPIE Vol. 5204, 35-40, 2003 .
8. Nascimento, S.M.C., Ferreira, F., and Foster, D.H. Statistics of spatial cone-excitation ratios in natural scenes. Journal of the Optical Society of America A, 19, 1484-1490, 2002.
9. http://personalpages.umist.ac.uk/staff/david.foster/Hyperspectral_images_of_natural_scenes_02.html